

Flow at ice-divide triple junctions: 2. Three-dimensional views of isochrone architecture from ice-penetrating radar surveys

Richard C. A. Hindmarsh,¹ Edward C. King,¹ Robert Mulvaney,¹ Hugh F. J. Corr,¹ Gisela Hiess,¹ and Fabien Gillet-Chaulet¹

Received 12 January 2010; revised 30 March 2011; accepted 13 April 2011; published 30 June 2011.

[1] Ground-based surveys of ice-divide triple junctions in two Antarctic ice rises, the Fletcher Promontory and Berkner Island, have been carried out using low-frequency ice-penetrating radars. These surveys have focused on understanding the internal layer architecture at and around the triple junctions, with a particular emphasis on understanding how the Raymond effect operates. A variety of features have been observed, including Raymond cupolas under the junctions, bump stacks of varying amplitude with distance from the divide, double bumps, crooked stacks implying divide motion, and the presence of ridges containing weak and strong bump stacks. It was generally not possible to elucidate the three-dimensional structure by correlation of pick crossovers, so instead a least squares cross-correlation technique was used which computes nominal age surfaces using radial basis function interpolation. Double bumps are absent from the central cupola of Fletcher Promontory, permitting us to infer that the ice here has thinned by around 500 m in the past 5000 years. Estimates of the age scale suggest that there will be recoverable Eemian ice. A technique for inferring the velocity profile at divides using layer traces and assumed velocities in the flanks is presented.

Citation: Hindmarsh, R. C. A., E. C. King, R. Mulvaney, H. F. J. Corr, G. Hiess, and F. Gillet-Chaulet (2011), Flow at ice-divide triple junctions: 2. Three-dimensional views of isochrone architecture from ice-penetrating radar surveys, *J. Geophys. Res.*, 116, F02024, doi:10.1029/2009JF001622.

1. Introduction

[2] An ice-divide triple junction is the junction point of three ice-divide ridges. Often such junctions are at summits, and we shall be focusing on these here, but they can also be found where ice-divide ridges bifurcate. In the introductory section of the companion paper [Gillet-Chaulet and Hindmarsh, 2011, hereinafter called Part 1], motivation for investigating ice domes and triple junctions at summits has been provided. In the remainder of that paper modeling of triple junctions and their associated isochrone architecture using the full system of stress equations and the Glen flow law was presented. Modeling on this scale has only become recently possible owing to increases in computing power. In this paper we present some detailed observations of the englacial radar layer architecture of triple junctions at Thyssenhöhe, Berkner Island, and the Fletcher Promontory, Ellsworth Land, using data obtained from extensive ground-based radar surveys. Actually, as will be seen, the architecture in these places is complex, and we use the results from Part 1 here to show what is understand-

able and what is not. A recent review of radar sounding is given by Bingham and Siegert [2007], while an example of shallow sounding of the three-dimensional structure is presented by Steinhage *et al.* [2005].

[3] A major motivation for these surveys was to look for Raymond arch stacks, which are sets of anticlines with vertically aligned apices lying beneath ice flow divides. Raymond [1983] first predicted these from modeling studies, and several ice divides have already been surveyed with ice-penetrating radar (Thyssenhöhe [Steinhage and Blindow, 1996], Dyer Plateau [Raymond *et al.*, 1996], Siple Dome [Nereson *et al.*, 1998], Taylor Dome [Morse *et al.*, 1998], Fletcher Promontory [Vaughan *et al.*, 1999], Roosevelt Island [Conway *et al.*, 1999], Hercules [Jacobel *et al.*, 2005], WAIS (see discussion by Conway and Rasmussen [2009]), Summit [Jacobel and Hodge, 1995], and Kealey Ice Rise and the Fuchs Piedmont Glacier [Martín *et al.*, 2009a]).

[4] Results from these surveys have been used to understand changes in ice-flow history [Conway *et al.*, 1999; Nereson *et al.*, 1998, 2000; Nereson and Waddington, 2002; Waddington *et al.*, 2005]. Particularly useful in this regard is the arch amplitude, and also the height at which the maximum amplitude is reached. For a given ice rheology, these two parameters provide information about the time of formation of the divide, and whether the ice thickness at the divide has subsequently changed. Martín *et al.* [2006] also

¹Physical Sciences Division, British Antarctic Survey, Natural Environment Research Council, Cambridge, UK.

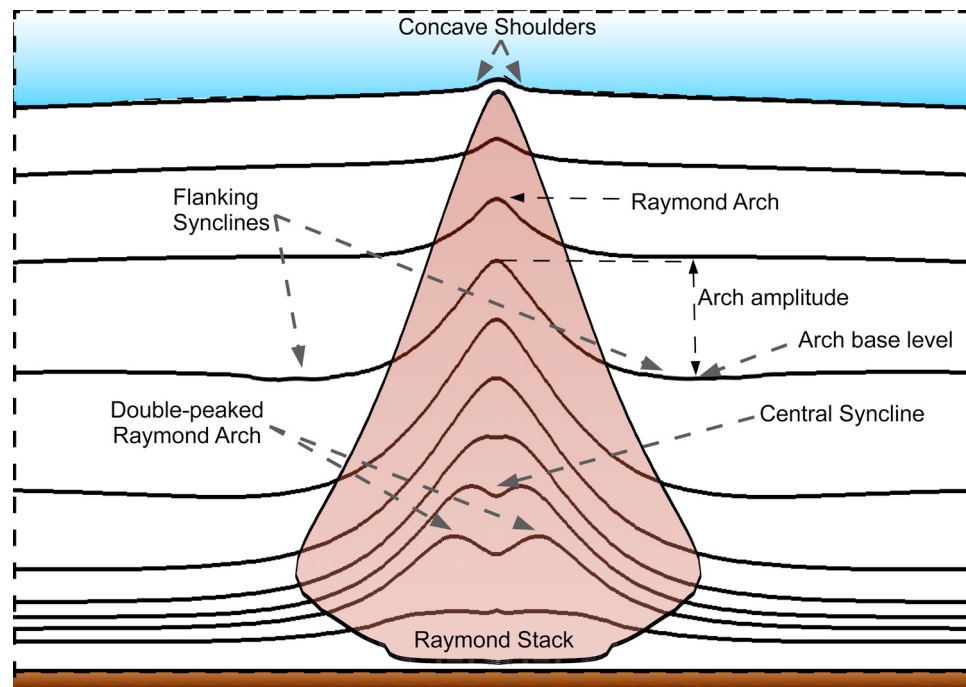


Figure 1. Cartoon illustrating terminology for stratigraphic features at ice divides. After *Martín et al.* [2009a, Figure 3].

show in some detail that it is possible to infer ice rheological properties, including temperature dependence, from the arch amplitude/arch base height curve.

[5] Figure 1 illustrates the various stratigraphical features to have been observed at ice divides, some of which arise from the nonlinear rheology of ice. It is already clear from modeling of relatively thin subtemperate ice masses that the Glen flow law cannot describe all that is seen. *Martín et al.* [2009a] consider three examples from West Antarctica; the Fuchs Piedmont Glacier, Adelaide Island; Kealey Ice Rise, Ellsworth Land, and the Fletcher Promontory. This latter example is considered in greater detail here. The focus of their interest is the double-peaked arches; the Raymond arch becomes two closely spaced anticlines, separated by a syncline. A further feature common to these stacks is the very large arch amplitude, which, if one assumes a Glen rheology to hold, indicate surprisingly high thinning rates. *Martín et al.* [2009a] show that by considering anisotropy in ice flow, one can simulate the double arches and the size of the arch stacks, and produce plausible representations of observations. *Pettit et al.* [2007], using different constitutive assumptions (i.e., the relationship between the stress and strain rate tensors), reach the same conclusions regarding the relationship between arch size and anisotropic flow. Indeed, the possibility arises that ice divides and triple junctions will provide strong constraints on constitutive relationships for ice, for example ice flow at low deviatoric stress [*Pettit and Waddington, 2003*].

[6] The geometry of triple junction surfaces is discussed in Part 1. We reiterate that domes generally comprise triple junctions, sometimes with three very strong ridges entering nearly symmetrically (the Fletcher being a very fine example) and more often, two stronger ridges entering which subtend angles of close to 120° , and one weaker ridge. Thyssenhöhe,

the south dome of Berkner Island, is an example of this. An obvious first question is how this surface structures affect the radar layer architecture, and how this affects interpretations of ice-flow history made from the architecture in this three-dimensional case. A likely significant effect is an increased horizontal plane shear stress along the ridge, which reduces the operation of the Raymond effect [*Martín et al., 2009b*]; see also Part 1.

[7] It has been noted that arches often have flanking synclines of smaller amplitude but simpler horizontal extent, and two theoretical discussions of these exist. *Parrenin and Hindmarsh* [2007, Figures 4 and 6] show that they can arise as a consequence of sharp horizontal changes in the ice viscosity, while *Martín et al.* [2009a] argue that they are a necessary consequence of anisotropy. It seems that a Glen flow law with $n = 3$ may have difficulty in producing these flanking synclines. However, since anisotropy tends to produce tall, stiff plugs, such a rheology necessarily produces sharp horizontal gradients in the viscosity and in consequence can induce flanking synclines. Anisotropy may be a sufficient but not a necessary condition for the formation of flanking synclines.

[8] The purpose of this paper is to present the results of the ice-penetrating radar surveys and to assess their glaciological significance in view of the modeling studies presented in Part 1. The surveys were aimed at producing a three-dimensional picture of the isochrone architecture. We use nearly all the data obtained, using an optimal method to correlate layers in different lines at crossovers. The paper plan is to (1) present topographic data on the surveyed areas (Fletcher, Berkner), (2) present radar layer data with an emphasis on the expression of the Raymond effect, (3) integrate this information into a three-dimensional description of the layer architecture, (4) compare this with theoretical pre-

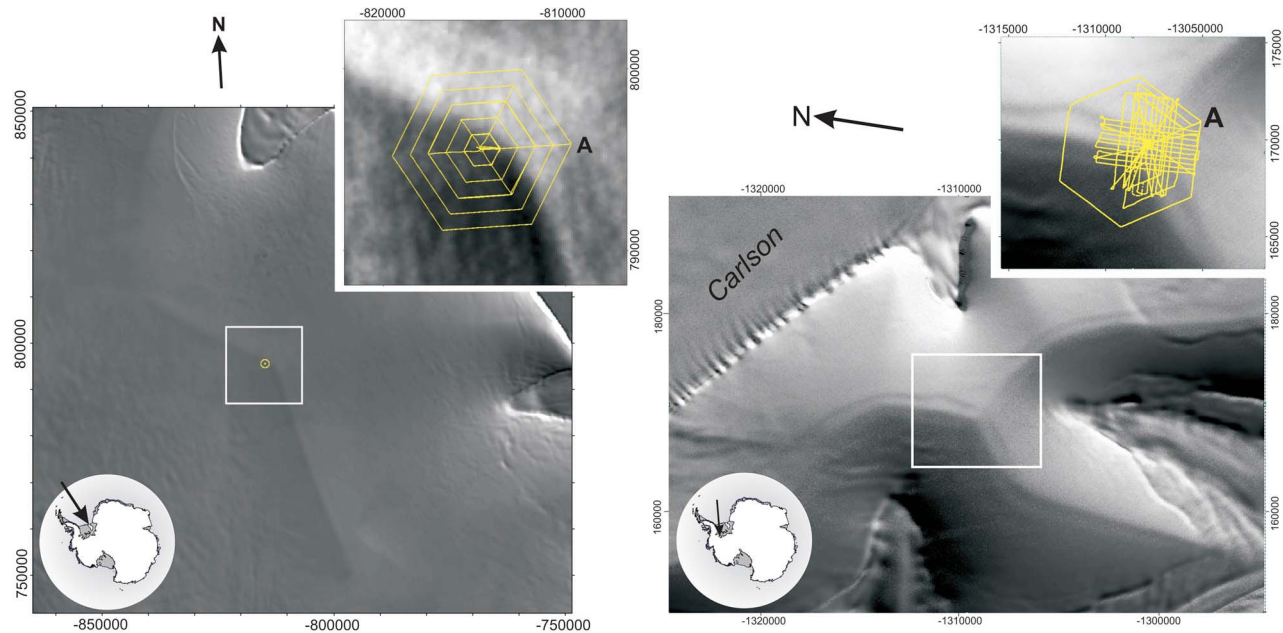


Figure 2. Satellite images of triple junction at (left) Thyssenhöhe, Berkner Island, and (right) Fletcher Promontory. Survey lines are indicated in yellow; the letter A indicates start and finish of hexagonal circuits. Berkner drill site is at the center of the spiders web survey pattern in the inset panel.

dictions, (5) make inferences about ice-flow history, (6) make a judgment about the best position for an ice core drill site in the Fletcher Triple Junction area, and (7) make an estimate of the age-depth curve for this area.

2. Data for Thyssenhöhe, Berkner Island, and Triple Junction, Fletcher Promontory

[9] Berkner Island, about 320 km long and 135 km wide, is an ice rise in the Weddell Sea sector of West Antarctica surrounded by the Ronne-Filchner ice-shelf system. Its highest point is Thyssenhöhe, where two ice cores have been drilled, most recently in 2004–2006. Thyssenhöhe has two clear divide ridges emanating from the flow center (Figure 2, left), subtending an angle of 136° . The bed beneath Berkner Island is entirely below sea level and is gently undulating. The ice thickness at Thyssenhöhe is over 900 m.

[10] The Fletcher Promontory is an ice rise 100 km long and up to 30 km wide situated on a horst block between the Rutford Ice Stream and Carlson Inlet. The elevation of the Fletcher Promontory triple junction is more than 800 m above sea level, and the ice thickness in the area is greater than 600 m. The bed gently slopes toward the Rutford ice stream until it meets the edge of the horst block [Lythe *et al.*, 2001]. The block is incised with three valley-shaped features, plausibly former cirque locations, two on the Rutford Ice Stream side and one on the Carlson Inlet side, which previous airborne ice-penetrating radar surveys have shown to be steep-walled [Lythe *et al.*, 2001]. The steep walls of the block fix the margins of the Fletcher Ice Rise, and create the circumstances necessary for three divide ridges to meet at the triple junction (Figure 2, right). The three arms meet at $120 \pm 1^\circ$.

[11] Both sites were surveyed with a 4 MHz nominal center frequency ice-penetrating radar. The BAS DELORES system

(Deep-Looking Radar Echo Sounder) is a monopulse radar capable of operating between 1 and 20 MHz. The transmitter comprised a Kentech pulse generator that produced ± 2000 V pulses at a repetition rate of 1 kHz. The data presented here were acquired with dipole antennae of 10 m length that have a nominal frequency of 4 MHz. The receiving system comprised an identical antenna pair coupled to a digital oscilloscope via a balun and amplifier. The sampling rate in a trace was 100 MHz. One thousand pulses were stacked for each trace, and the trace spacing was between two and three meters. Triggering was by air-wave from the transmitter.

[12] Position, elevation and radar returns were measured on the Fletcher Promontory in December 2005, on eight separate days, at the positions indicated in Figure 2 (left), which comprised 221 km of survey lines. Line topology consisted of a standard square grid, mainly on the southern side of the triple junction, as well as hexagonal lines centered on the triple junction which crossed the divide-ridge arms. The same radar system was used to survey the area around Thyssenhöhe on five separate days in February 2006. In this case, the survey topology consisted of five concentric hexagons, separated by 1 km, centered on the drill site, which is about 3 km from the summit of Thyssenhöhe. Total survey line length was about 100 km.

[13] In both sets of surveys GPS readings were taken every second. A failure of the dual frequency system meant that positioning returns were only obtained from the single frequency system, with the consequence that the GPS data could not be postprocessed, degrading in particular the surface elevation data. As the ice surfaces were very smooth, we were able to make an assumption that elevations were continuous, and had no cliffs. Large jumps of the order of 1–5 m in the data were removed so that elevations on either side of the apparent jump were consistent. Observations at crossovers

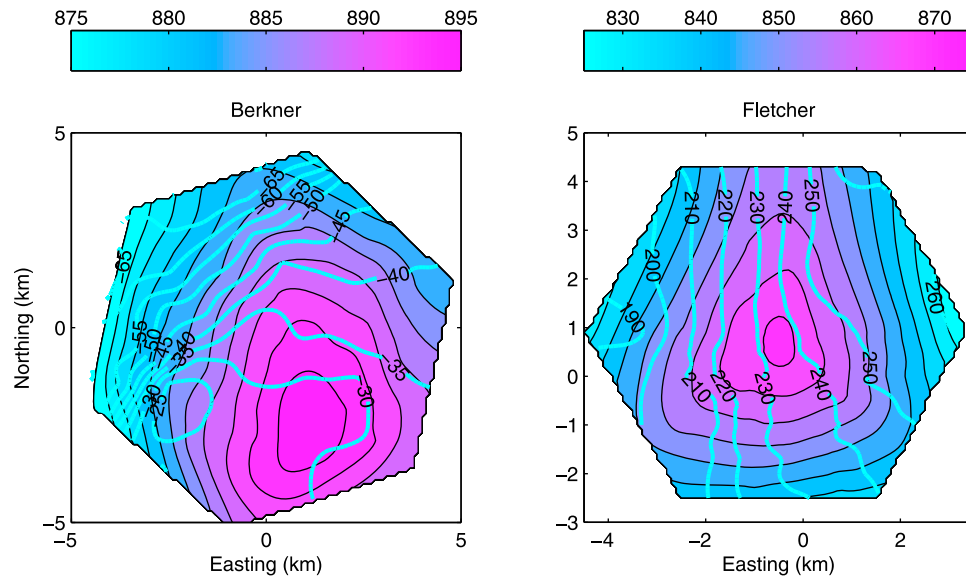


Figure 3. Surface (color coding) and bed contours (light blue lines) in meters derived from ground-based GPS measurements and ice-penetrating radar: (left) Berkner and (right) Fletcher.

showed that readings from different days had different mean heights, and that there were also trends over individual days. They were removed by detrending with quintic polynomials, and the resulting surface interpolated using radial basis functions to produce the surfaces seen in Figure 3.

[14] A brief exposition of radial basis functions is given in Appendix A. Radial basis functions are an efficient way of interpolating nonnoisy scattered data. Error estimates for the actual interpolation are difficult to obtain, but are likely to be small compared with the geophysical measurement errors.

[15] These surfaces represent our best approximation to the ice sheet surface, and they are accurate to better than 10 m. Comparison with a recent satellite DEM [Bamber *et al.*, 2009] indicates a difference in mean height of about 20 m. The difference between the demeaned traces gives RMS differences of a few meters, with the differences mainly occurring with a wavelength of the divide ridge features. In all cases the interpolated satellite DEM appears to be smoothing the divide ridges, so we believe that our greater relief is a more accurate representation of the topography.

[16] Comparison of the actual route to the planned route shows errors on the straight sections of around 10 m. These are the sum of our geodetic GPS errors, the navigation GPS errors, and the navigation of the skidoo. Thus, a very conservative estimate of the error of the horizontal location is 10 m, but we suppose it to be much less. Jumps in horizontal position were not found. The error in horizontal position is less than one percent of the horizontal scale of the features we are interested in.

[17] Radar-data processing involved bandpass filtering, a gain function, a two dimensional (2-D) median filter to remove noise spikes and Kirchhoff migration. No further stacking was employed. We used a constant wave speed of 0.168 m ns^{-1} for migration.

[18] Following processing, the bed and visible internal reflections were picked. Only layers with good continuity

were picked. Picking of the bed produced good thickness matches at crossovers with maximum errors of the order of 3 m, which were used with the surface data to produce a map of the bed for both survey sites in Figure 3. While the bed at Fletcher slopes gently in line with the general trend, the bed at Berkner shows more pronounced relief. Observed layer thicknesses are of the order of 5 m, which is an estimate of the accuracy of the picked depth. This is also an estimate of the accuracy of the interpolated layer elevations discussed below.

[19] For the correction of Fletcher and Berkner layer depths, density profiles from ice cores are used. Density measurements to a depth of 80 meters from an ice core taken at Berkner Island are available [Gerland *et al.*, 1999; Mulvaney *et al.*, 2002]. For Fletcher Promontory, the closest ice core available, ITASE01-5 [Kaspari *et al.*, 2004], is at a distance of 300 km and has density measurements reaching down to 115 meter depth. Polynomial curves are fitted through the density *versus* depth data with the constraint that a density of 918 kg m^{-3} is reached at 150 m for Fletcher and 120 m for Berkner case, following the methodology of Hempel *et al.* [2000]. The total depth correction from the firm column for Fletcher is 8.17 m and for Berkner 7.45 m, in comparison to using a uniform wave speed. Appropriate corrections were applied to picked layers located within the firm layer.

3. Analysis and Interpretation of the Radargrams

[20] Figures 4, 5, and 6 show the radargrams, processed as described above, with clear examples of Raymond arches. As well as the obvious isochrones, there are some horizontal artifacts which are noise from the radar equipment. Figure 4, which is of the outer survey hexagon from the Fletcher Promontory, crosses the three divide arms, showing the double-arch features first noted at Fletcher and Kealey Ice Rise [Martin *et al.*, 2009a]. In addition, flanking synclines

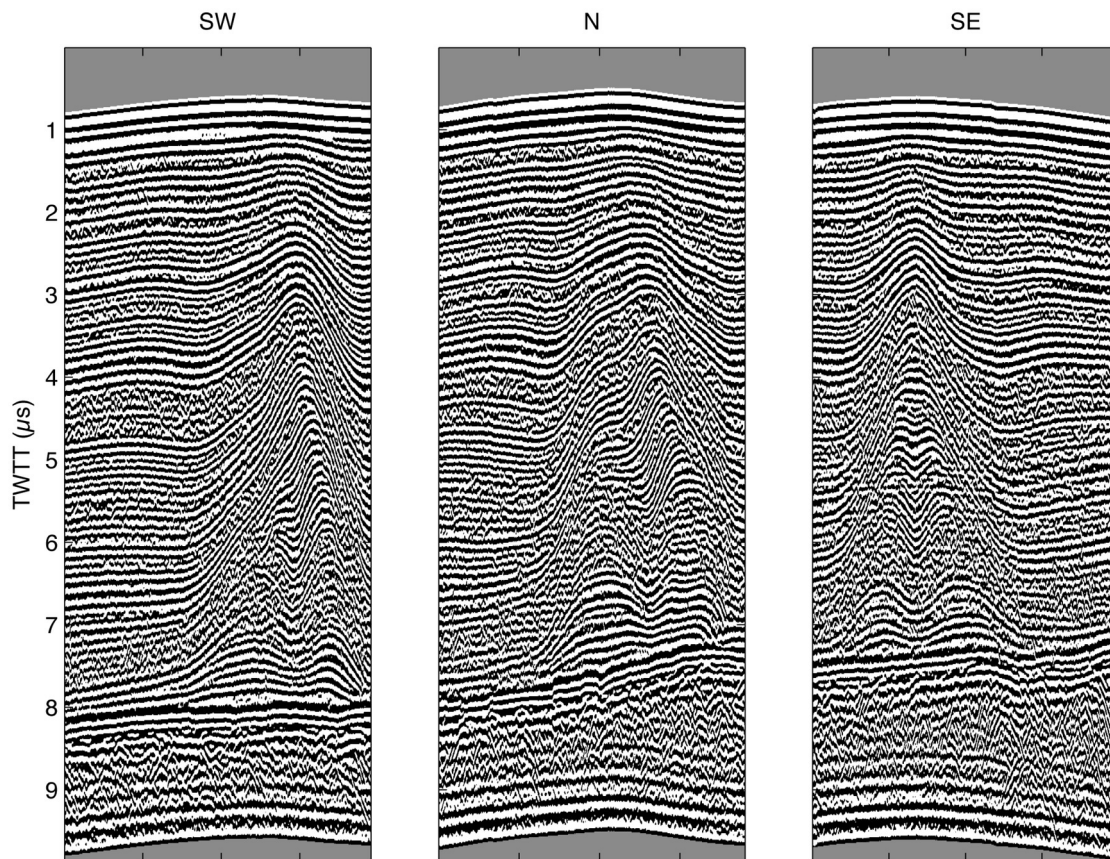


Figure 4. Radargrams across the three indicated arms of the divide ridges joining the Fletcher triple junction. Survey lines taken from outer hexagon (Figure 1). Note the very high amplitude of single bumps, flanking troughs, and presence of double bumps and tilted axes of apices. All views have the western side on the left. The sections are 4 km long.

are seen. The arch stack in the SE arm is essentially symmetrical and underneath the ridge top, while the other two stacks are crooked and not exactly under the ridge top, suggesting recent migration of the divide. The arches are very large, and oversized by 50% compared with steady arches predicted using a Glen rheology. One possibility is very rapid recent dynamic thinning [Conway *et al.*, 1999], but Martín *et al.* [2009a] provide an explanation as to why double arches form, and suggest that they are associated with oversized arches, showing that rheological models which incorporate anisotropy can produce these features. Figure 5 shows a radargram from a line which crossed the triple junction. Again there is a prominent Raymond stack, with flanking synclines but no double arches. The size of this arch and the implications for ice dynamics are discussed in section 4.2.

[21] Figure 6 shows the outer hexagon from Thyssenhöhe. There is one very prominent Raymond arch stack in the southwest arm, and a possible but very muted feature corresponding to the north arm (recall that there is no third arm).

[22] Figure 7 shows picks from the Fletcher triple junction survey as line plots in three-dimensional space. The outer hexagonal survey (Line d19_1) is used as a frame in all of the figures. Picked layers which crossover at around the same height from four other lines are also shown in the four panels. The d15_1/d19_1 (Figure 7a) combination shows

that the arch stacks associated with the SW and SE arms decline in size as one moves centrally toward the summit. This also seems to be the case with the north arm as indicated by the d18_1/d19_1 panel (Figure 7c), although the survey density is substantially sparser here. The other two panels (d16_1/d19_1 (Figure 7b) and d05_2_ew/d19_1 (Figure 7d)) confirm this story and also show that the central cupola stack is separate from the arm arch stacks.

[23] It is clearly desirable to aggregate all this geometrical information, and we describe here how this may be done. The usual way is to identify crossovers for individual layers, but this was not consistently feasible. One reason was that we could not carry out a three-dimensional migration, which led to inconsistencies in the layer elevation. An operational reason was that for a given survey line, layers were picked on the basis of their horizontal continuity, which meant that the most suitable layer for picking was not the same for each survey line. This seemed principally to arise from variations in return power that arose from different snow conditions. In consequence we require a procedure which links picks from each survey line at crossovers. We therefore adopted a procedure, described in Appendix B, which determines the least square optimal estimate of the isochrone field, by computing the optimal correlation of layers at the crossovers.

[24] To do this, internal radar layers were labeled with their mean normalized depth, giving the layer a “nominal

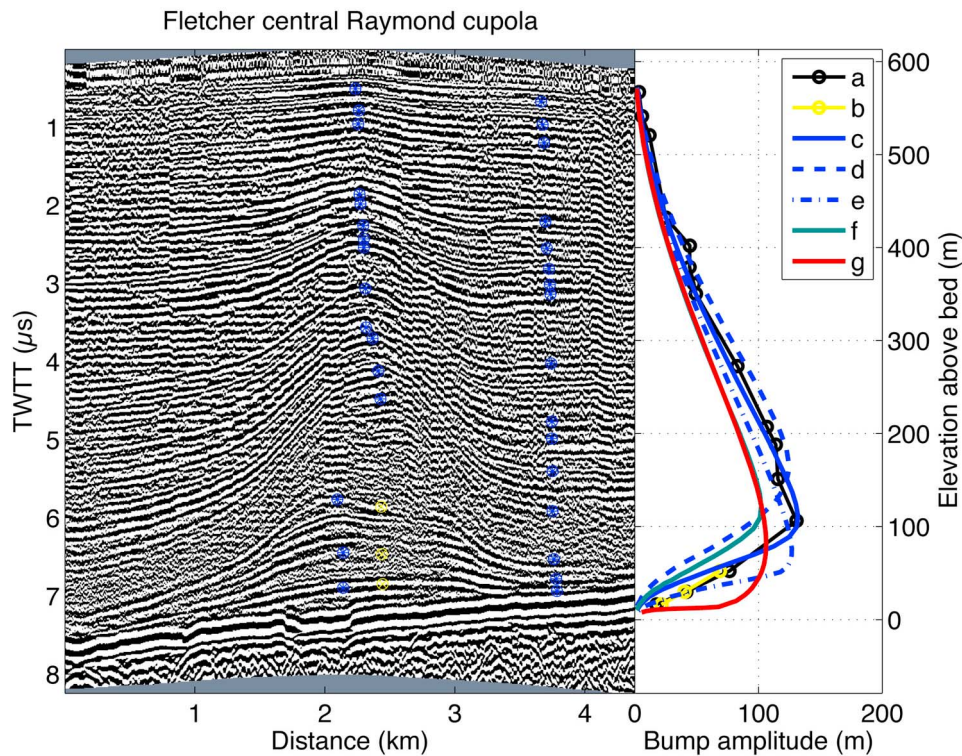


Figure 5. (left) Radargram across the summit of Fletcher triple junction. Note the absence of double bumps, tilted apex axis, and flanking troughs. Western side on the left. Crosshairs show picks of layer amplitude. (right) Plots of arch amplitude against elevation (a and b), with alternative picks shown in yellow, and modeled results (c–g). All modeled results use Glen index $n = 4$ with axisymmetric geometry, apart from result f, which has $n = 3$. Result c is best fit, with thinning rate of 0.1 m/yr over 5000 years; result d is thinning rate of 0.2 m/yr over 2500 years; result e is thinning rate of 0.05 m/yr over 10,000 years; result f is $n = 3$, with thinning rate of 0.1 m/yr over 5000 years; and result g is no thinning, steady state solution.

age” for each survey line. Radial basis functions are used to interpolate *vertically* between layers (but not extrapolate to deeper than the lowermost layer), giving a nominal age field from the surface to the deepest observed radar layer. An example is shown in Figures 8a and 8b. It can be seen that the interpolation, which includes a slight smoothing, provides a credible representation of the nominal age field above the lowermost layer.

[25] By this construction, the nominal age of a layer is a property of each survey line. To obtain a global value, that is, a consistent age field for all lines, the nominal ages for each survey line must be correlated at each crossover. The next step therefore is to compare the nominal ages with those for other lines. The aim is to compute a nominal age field for each survey line, which is a linear ratio of the nominal age field for every other line, and which minimizes the errors at the crossovers. Thus, the age at any normalized depth for any one line is simply a proportionality factor (scaling factor) for that of any other line. A least squares formulation which allows for errors in the nominal age in both the survey lines involved at each crossover to create a global best estimate of the nominal age field is described in Appendix B. The solution is the optimal scaling between the nominal ages of individual survey lines that minimizes the errors at crossovers. We could in principle have generalized the linear scaling to a polynomial relationship, and this would

have improved the match, but for our present purposes, which is depicting the layer architecture, this step did not appear necessary.

[26] Examples of the crossovers for two survey lines are shown in Figures 8c and 8d. Note that this correlation is constructed for each intersecting survey line pair, and the correlation is consistent between all pairs. To expand on this further, knowing the scaling factor between one line and two further lines allows inference of the scaling between these latter two lines. Figure 8d in particular shows the optimal linear regression between the two lines, and the observed correlations. Three-dimensional nominal age fields are then created by radial basis function interpolations along surfaces of constant *normalized* height. This is motivated by the observation that radar layers in areas where the accumulation is spatially uniform tend to lie along surfaces of constant normalized height [Parrenin *et al.*, 2006], even when horizontal advection is present and the thickness is varying over length scales greater than the ice thickness.

[27] Interpolated surfaces with the same nominal age are approximate representations of isochronic surfaces subject to errors introduced by the process. Apart from picking errors, the main sources of error are in the interpolations, and principally the correlation at the crossovers.

[28] The three-dimensional architecture is illustrated in Figure 9 by showing an isochronic surface at around 0.6 of

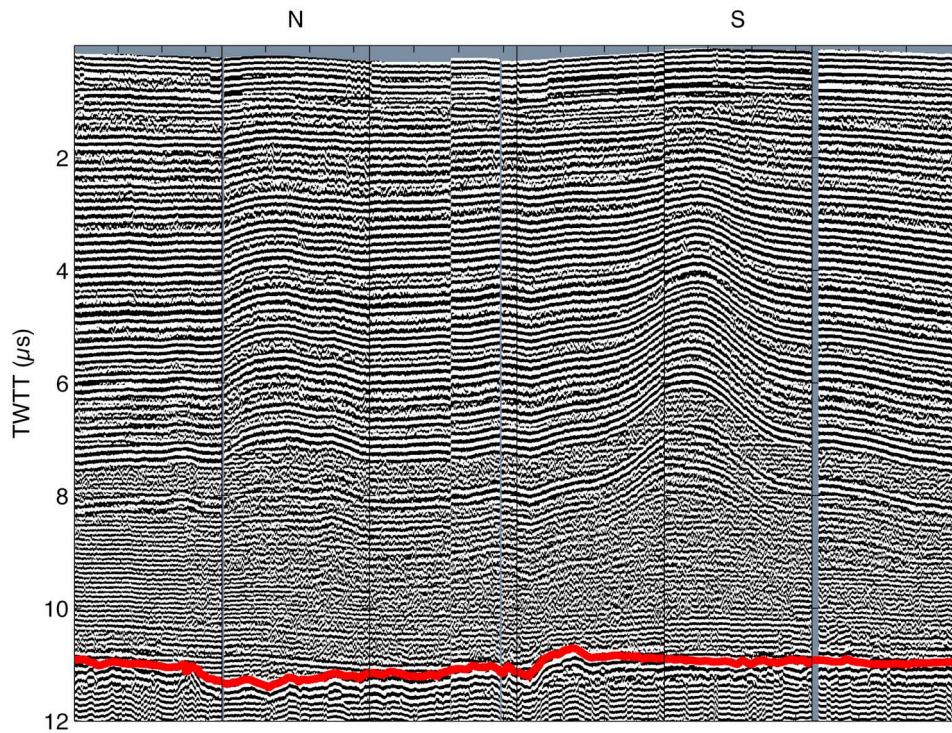


Figure 6. Radargram around outer hexagon survey line at Thyssenhöhe, Berkner Island. Note one large Raymond arch stack, a possible second one (third panel from left), the relative small amplitude of bumps, and the absence of flanking troughs. Views from outside of hexagon. Panels are 5 km wide. Red line is bed pick.

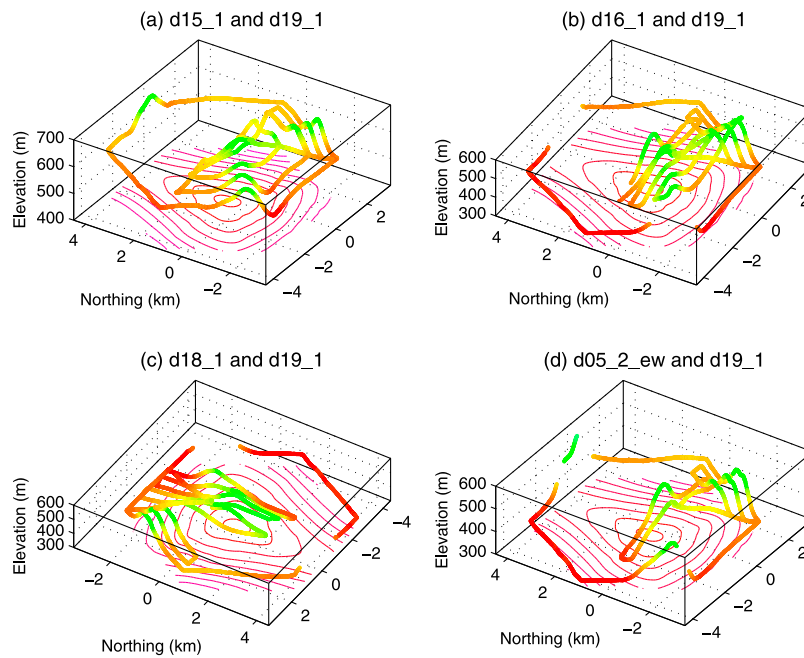


Figure 7. (a–d) Picked radar lines for the Fletcher Promontory shown in three dimensions. Labels indicate survey line number. All panels show outer hexagonal survey line (d_19_1) and one other line. Viewing angle varied to show three-dimensional structure; note in particular that Figure 7c is at a reverse angle. Elevations are color-coded for display purposes: lime green is higher and orange is lower. Ice surface contoured in red for display purposes on diagram bases, with 5 m interval.

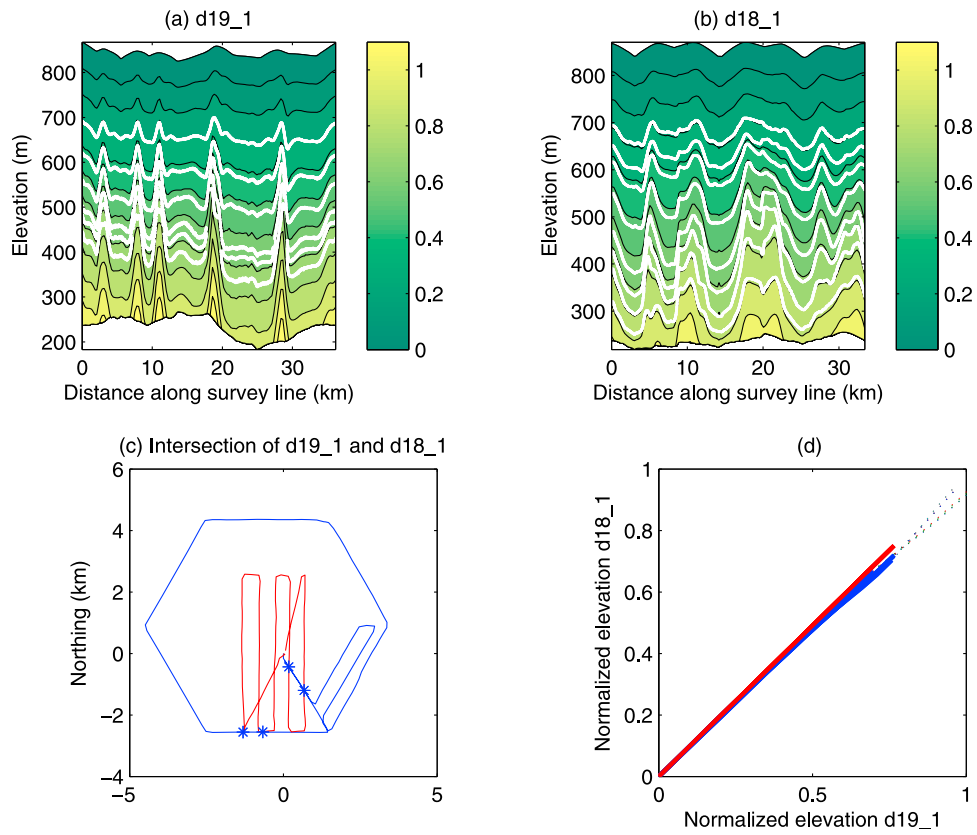


Figure 8. Illustrating the cross-correlation procedure. (a and b) Picked lines (white) and interpolated and extrapolated “nominal ages” for two lines (filled contours). Extrapolated nominal ages beneath the lowest pick are not used. (c) Crossover points of the two lines. (d) Plots of nominal age against nominal age for all the crossovers of the two lines (blue, essentially coincident), as well as the best linear regression relationship (red). The dotted line is the extrapolated value. This best estimate also includes information from all the other cross correlations.

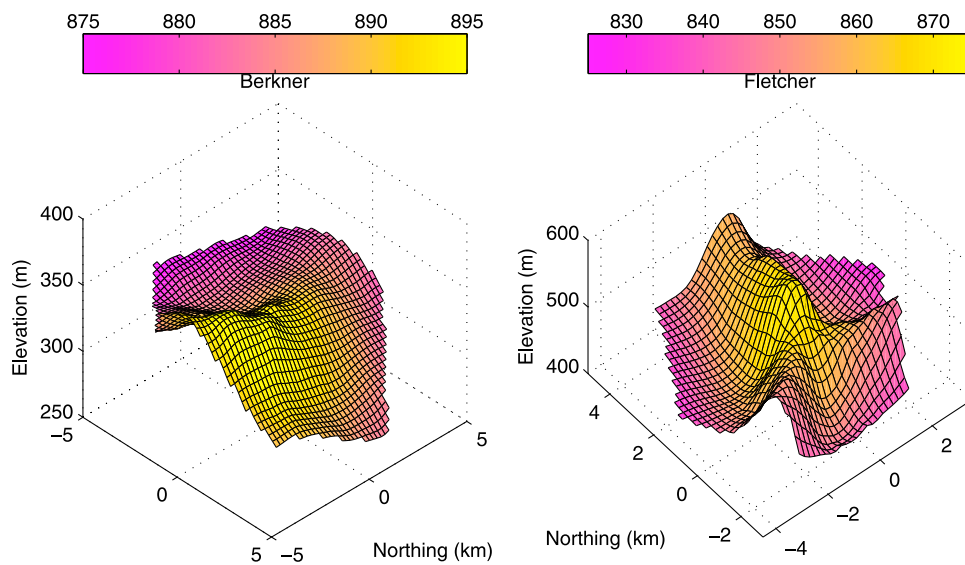


Figure 9. Interpolated isochrone surfaces for (left) Berkner and (right) Fletcher, at mean normalized depths of approximately 0.6. Color coding on isochrone represents the ice upper surface elevation in meters.

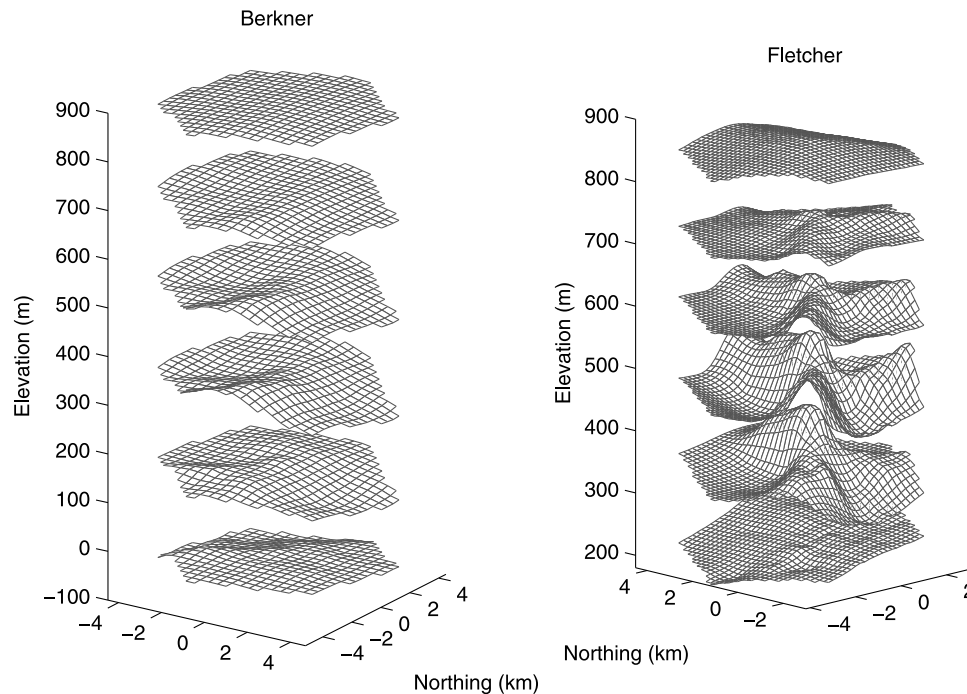


Figure 10. Interpolated isochrone surfaces for (left) Berkner and (right) Fletcher, at mean normalized depths of approximately 0.2, 0.4, 0.6, and 0.8. Above them is shown the ice upper surface, and at bottom the bed is shown.

the normalized depth, for both survey sites. They are also shown in their context of other such isochronous surfaces, and the ice surface and bedrock, in Figure 10. Berkner clearly has one significant Raymond arch stack, extending from near the center along the SW arm. The amplitude of the arch under the summit of the ice rise is no bigger than on the arm. There is a second arch-like feature exiting along the north arm, but it is muted and it is not clear whether it can be unequivocally called a Raymond stack. A third notable feature is the strong eastward dip in the layers on the east of the summit. This feature seems likely to extend beyond the survey area. We suppose it to be due to an accumulation rate gradient.

[29] The structure at Fletcher is more complex. At the edge of the hexagonal survey area, there are three significant arch stacks corresponding to the divide arms (Figures 9 and 10). These arches are very large with high amplitude, and the arch stacks all contain double arches (Figure 4). However, the amplitude of these arches declines toward the summit; in the immediate area of the summit, we see a stack of Raymond cupolas (i.e., three-dimensional arches). There are no double peaks in the cupola stack, though there are also clear flanking synclines. The cupola stack is not exactly axisymmetric, seeming to stretch somewhat along the north arm, but the amplitude does clearly decline in this area, as can be seen by inspecting the original picked data (Figure 7).

4. Discussion

4.1. Berkner Island

[30] The implications of the structure of the SW divide ridge for Berkner Island are analyzed and discussed in the context of the post-LGM glacial history of this ice rise by *Mulvaney et al.* [2010], who tie in these data with gas and

isotope data obtained from an ice core extending to the bedrock. They show that the arch amplitude/arch height distribution is consistent with the idea that the SW arm in the vicinity of Thyssenhöhe reached its present position about 4000 years ago, which their interpretation of the ice core data indicates to be the time when Berkner Island stopped thinning. Whether the very much more muted feature under the north arm is a Raymond arch, and why the cupola amplitude under the summit is at best no greater than the arm arch amplitudes, since the predictions in Part 1 suggest it should be rather larger, are perplexing questions. Taken together with the evidence from the SW arm that suggests that overall elevation has not changed in the past 4000 years, we infer that there has been migration of the north arm.

[31] The two most plausible hypotheses are the greater surface slope directed along the north arm, causing the operation of the Raymond effect to be damped [*Martin et al.*, 2009b] and the mutually inclusive idea that the north arm has been migrating westward, cutting into the SW arm and forcing the summit to move westward as well.

4.2. Fletcher Promontory

[32] The most notable feature of the Fletcher surveys is the central cupola stack in the layer architecture, showing no double arches, compared with the three larger arch stacks underneath each of the three ridges emanating from the summit, which exhibit large and clear double arches as well as evidence of divide migration in two of the three arms. This is apparently inconsistent with the modeling of Part 1, who, using a Glen rheology, showed that the arch amplitudes are expected to decline along arms, and certainly not to be greater than in the cupola.

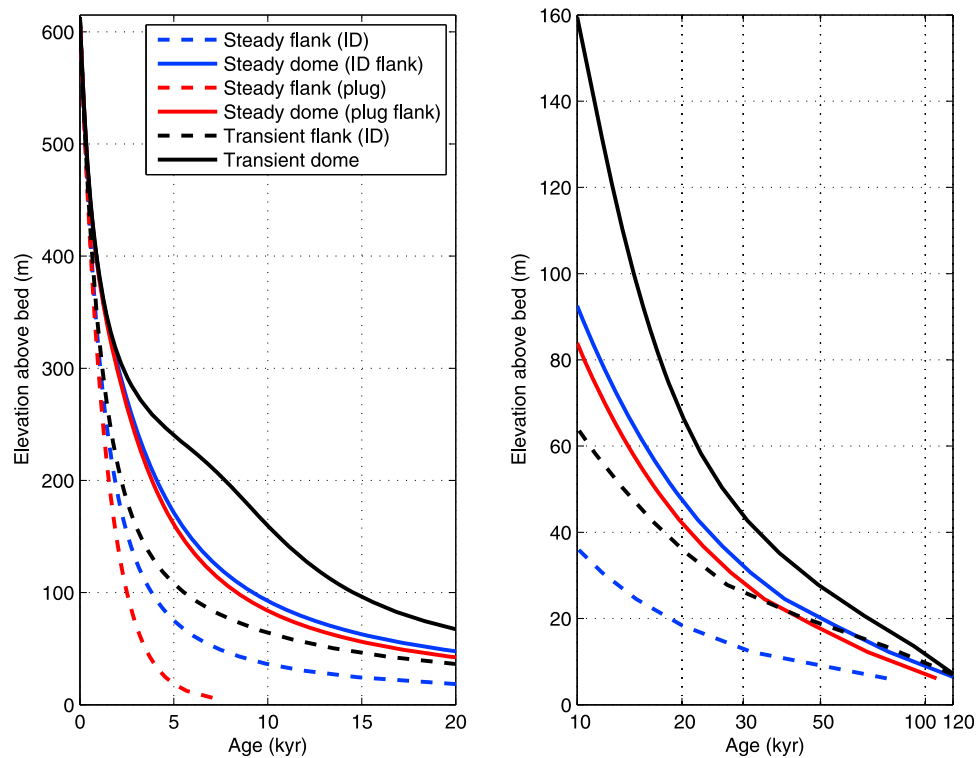


Figure 11. (left and right) Predicted Fletcher timescale. Figures 11 (left) and 11 (right) show different details; note the logarithmic timescale in Figure 11 (right). Constant accumulation rate of 0.45 m/yr is assumed [Woodward and King, 2009]. Solid lines represent age at dome center, and dotted lines represent age in the flank. Black lines are for a scenario with a Glen index of 4 and a thinning of 0.065 m/yr starting at 5000 years B.P. Red and blue lines are for shape functions derived on the assumption that the dome is in a steady state; red and blue refer to assumptions that the flank is experiencing plug flow or internal shear (ID) with $n = 4$.

[33] If we follow the analysis of *Martin et al.* [2009a], who suggest that double arches form when a divide has been present in a location for a considerable period (specifically, three to four times the advective timescale given by the quotient of ice thickness and accumulation rate; this timescale is about 1400 years for the Fletcher Promontory) then we are immediately faced with the question as to why the arm ridge size decreases and vanishes toward the central summit, and why the central cupola stack does not show double arches. If double-arch formation is purely a consequence of divide age, the implication is that the summit location has peregrinated, while at a distance of 3 km and beyond from the summit, the divides have had a fixed location. While this is in principle feasible, it would require a somewhat specific forcing associated with changes of elevation in the three inlets which cause the triple junction to exist (Figure 2, right).

[34] An alternative is to suggest that the hypothesis of *Martin et al.* [2009a], that double arches are due to anisotropification is correct, but that the theory requires modifications. Specific suggestions, which are in accordance with the observations at Fletcher Promontory, are as follows.

[35] 1. Along-ridge shear stresses play a significant role in the anisotropification process, leading to large Raymond arches with double peaks, perhaps with the major effect of speeding up the process. This is consistent with the observation that arch sizes grows with along-ridge surface slope as one moves from the summit.

[36] 2. The different symmetries in the strain rate at a summit compared with those at a divide affect the fabric formation process. They are not mutually exclusive, and it is not clear that both are necessary.

[37] With these ideas, we suggest that the central cupola stack at Fletcher Promontory has not been affected by processes of anisotropification, at least to the extent of double bumps forming, either as a consequence of time or physics, noting its similar appearance to the layer architectures obtained in Part 1 with a Glen rheology, that is, the much greater amplitude at the summit, and the rapid decline away from the summit.

[38] We now show that the arch amplitudes are consistent with a choice of Glen rheology. Figure 5 shows a plot of arch amplitude against height from a survey line crossing central dome near the summit, as well as a fit from one dimensional modeling with a Glen, $n = 4$, rheology.

[39] The modeling is carried out using finite element computations of vertical velocity shape functions (Part 1) in a simple one-dimensional finite difference model. The evolving age equation is solved both at the divide, and in the flank, ignoring horizontal advection which is small. The shape function, that is, the vertical velocity distribution with elevation normalized by the surface velocity, is to a good approximation (relative error is the ice surface slope) independent of ice thickness [Wilchinsky and Chugunov, 1997; *Martin et al.*, 2009b]. This is true for both divide and flank.

The surface velocity is set to the sum of the accumulation rate and the rate of change of ice surface height. These velocity distributions are used to compute the downward movement of ice, in association with the prescribed choices of thinning rate of the ice and accumulation rate. This is exactly the procedure used by *Conway et al.* [1999] to investigate the glacial history of Roosevelt Island. The best fit shown in Figure 5 occurs with a divide-formation time of 5000 years B.P. and a mean thinning rate of 0.1 m/yr, implying a total lowering of 500 m. Other model results are shown to illustrate that the robustness of the result. The relatively high rheological index is consistent with other findings [e.g., *Martin et al.*, 2006]. We note that simple application of this method to the much larger arches on the divide arms required thinning rates of greater than 0.1 m/yr over periods of between 3000 and 6000 years and do not explain the double arches. We suppose that the arch stacks along the arms have been strongly modulated by anisotropification and provide no information about thinning histories under current states of theoretical development. Our results are consistent with thinning histories deduced by *Bentley et al.* [2010] from exposure age dating in the Ellsworth Mountains.

[40] Finally, we can use the traced layers from radargrams crossing near the summit to estimate an age-depth timescale. We suppose that in the flanks, away from the Raymond cupolas, the flow is adequately described by the shallow-ice approximation, and use this, along with suitable hypotheses regarding the ice thinning, to compute an age depth relationship. Our main concern is investigating whether the LGM is expected to be seen in the ice core record. We adopt a conservative approach by ignoring the likely decrease of accumulation rate during the most recent glacial period, and consider three cases: (1) the thinning scenario mentioned above, or, an assumption that the arch is a steady feature, with flow in the flank described either by (2) plug flow, or (3) internal deformation, with a Glen index of 4. In this case, we have to derive a velocity field that is consistent with the arch amplitude as a function of depth (which depends on the flank flow assumptions). The method, which is purely empirical, is described in Appendix C. This method is a subset of a more general method for tracing shape function variations proposed by *Rousselot et al.* [2009].

[41] Figure 11 shows computed timescales in flank and divide areas. As expected, the ice is considerably older in the arch. The difference between the black and blue solid lines shows how older ice remains at higher elevations as a result of thinning. The downward kink in the transient dome calculation is due to the formation of the ice divide. LGM ice (here defined as 17 ka B.P.) is predicted to lie at 80 m above the bed. Below that, ages are speculative as the accumulation rate has almost certainly changed, but the indications are that ice from the last interglacial and possibly ice from the preceding glacial stage may be found. This possibility is enhanced by the flat bed, which will mitigate against flow complications leading to folding.

[42] Some more recent change is indicated by the fact that there is a clear tilt, interpreted as a migration signal of the divide westward, in the north and SW arms, consistent with the observations of *Vaughan et al.* [1999] farther north. While it would be pleasing to use this as a signal of the relative increase of the elevation of the Rutford Ice Stream

compared with the Carlson Inlet, it is clear that the story is likely to have been complicated by ice dynamics in the small inlets which delimit the Fletcher Promontory triple junction.

5. Conclusions

[43] 1. Surveys at Thyssenhöhe and the Fletcher Promontory triple junction show that low-frequency ice-penetrating radars (4 MHz) provide effective means of surveying Antarctic ice rises in order to yield three-dimensional structure.

[44] 2. Optimal techniques which do not rely on one-to-one correlation of radar layers at crossovers can be successfully used to construct three-dimensional geometric representations of layer architecture.

[45] 3. Neither surveys provide layer architectures which are easily explicable in terms of ice masses with a Glen rheology flowing in a steady state.

[46] 4. The Berkner survey shows one very strong Raymond arch ridge, which started forming around 4000 years ago. The second arm is very muted, but may be younger or the Raymond effect may be damped by higher shear stresses.

[47] 5. The Fletcher survey shows a very clear central stack of Raymond cupolas, which decay very rapidly in amplitude with distance from the summit. These show no evidence of anisotropic flow in the central cupola. Dating suggests that the summit occupied this position about 5000 years ago, and has been thinning with a mean rate of 100 mm/yr.

[48] 6. At distances greater than about 3 km from the summit, a different set of Raymond arch ridges forms under the three divide arms at Fletcher. These have much greater amplitude than the cupola under the summit, and are double peaked. We concur with the suggestion of [*Martin et al.*, 2009a] that the special features under the arm ridges are likely to be due to the development of fabric, but suggest that the theory may need to be modified to represent what is seen at Fletcher Promontory. In particular, ideas that divides with shoulders are “old” divides need to be treated with caution while the role of along-ridge shear remains uncertain.

[49] 7. By tracing radar layers from areas believed to be described well by the shallow ice approximation to an area under the summit proposed as a drill site, we have obtained a preliminary age-depth scale, which suggests that LGM ice will be at 80 m above the bed, with the strong possibility that ice from the last interglacial can be recovered.

Appendix A: Radial Basis Function Interpolation

[50] Radial basis functions are discussed by *Buhmann* [2003]. The theory of interpolation errors for these functions is still under development and is difficult to apply [e.g., *Lowitzsch*, 2005], so we do not quote errors for the actual interpolation.

[51] Consider a set of N points randomly scattered in a D -dimensional space with coordinates $\mathbf{r}_i = (r_1, \dots, r_D)$, $i = (1, N)$, with a field value of u_i . We wish to compute the interpolated field $u(\mathbf{r})$. The radial basis function is defined in terms of a function $\phi(\mathbf{r} - \mathbf{r}_i)$; at the moment the choice of ϕ is fairly general. We write

$$u(\mathbf{r}) = \sum_i^N \gamma_i \phi(\mathbf{r} - \mathbf{r}_i) + \mathbf{c} \cdot \mathbf{r} + c_0$$

where \mathbf{c} is a D -dimensional vector. The unknowns are γ_i , \mathbf{c} and c_0 . We find N equations

$$u(\mathbf{r}_j) = \sum_i^N \gamma_i \phi(\mathbf{r}_j - \mathbf{r}_i) + \mathbf{c} \cdot \mathbf{r}_j + c_0.$$

We close the system with the equations

$$\begin{aligned} \sum_i^N \gamma_i &= 0, \\ \sum_i^N \gamma_i (r_j - r_i) &= 0, j = (1, D). \end{aligned}$$

which ensure that the data values are respected by the interpolation at the data point locations. This defines a linear equation with order $N + D + 1$ with unknowns γ_i , \mathbf{c} and c_0 . A heuristic smoothing may be constructed by subtracting an operationally determined smoothing parameter from the diagonal entry of the first N rows. We use a Matlab code written by A. Chirokov (2006, <http://www.mathworks.de/matlabcentral/fileexchange/10056-scattered-data-interpolation-and-approximation-using-radial-base-functions>). The linear radial basis function $\phi = r$ was used.

Appendix B: Creation of Three-Dimensional Nominal Age Field

[52] In this appendix we describe in detail how the picked lines are converted into a nominal age field. A nominal age field is one where ice of the same age is labeled with the same number; this number bears no relation to the real age, and additional assumptions or data need to be introduced to assign a physical age. The procedure described in this appendix determines the least squares optimal estimate of the isochrone field, which automatically creates the optimal correlation of layers at the crossovers.

[53] Once the lines have been picked, they are each labeled; their nominal age is simply the spatial average of the mean normalized height ζ . This is defined as the distance above the bed b divided by the thickness H , or

$$\zeta = \frac{z - b}{H}.$$

Radial basis function interpolation is then used to interpolate the nominal age between layers, but not to extrapolate below the deepest layer. These interpolants are computed at a fixed set of normalized elevations. The number of normalized elevations chosen needs to be sufficient to ensure that all picked layers are represented.

[54] The next step is to compare the nominal ages with those obtained similarly for other lines. The aim is to compute a nominal age field for each survey line that minimizes the errors at the crossovers. If our data and picking were perfect, and we were able to pick the same layers in all the lines, then we would be able to reduce this error to zero. Where these conditions cannot be met, the optimal nominal age field we compute will not be the same for the two lines at the crossovers.

[55] We have M crossover points; at each crossover point j there are g_j elevations where correlations of age can be made

between the survey lines. The total number of correlatable elevations is given by

$$N = \sum_{j=1}^M g_j.$$

At each crossover we seek to correlate two age fields, creating a global objective function

$$J = \frac{1}{2} (\mathbf{Z} - \mathbf{Z}^*)^T \mathbf{C}_{\mathbf{Z}^* \mathbf{Z}^*}^{-1} (\mathbf{Z} - \mathbf{Z}^*) + \lambda^T (\mathbf{J} - \mathbf{A}) \mathbf{Z},$$

where the last term is a linear constraint, described below, and where \mathbf{Z} , our solution, is a column vector of

$$\zeta_{ijklm}$$

which is the i th vertical point at the j th crossover of survey lines k and ℓ . The final subscript $m \in (1, 2)$ indicates whether we are considering the k or ℓ lines, respectively. Under perfect conditions (no data errors, all layers cross-correlatable) we would have $\zeta_{ijk\ell 1} = \zeta_{ijk\ell 2}$. The vector \mathbf{Z} is formed by column-wise concatenation of $\zeta_{ijk\ell 1} = \zeta_{ijk\ell 2}$. The vector \mathbf{Z}^* is formed from the values computed at the g_j points from vertical interpolation of the nominal ages from the picks. The covariance matrix is denoted by $\mathbf{C}_{\mathbf{Z}^* \mathbf{Z}^*}$.

[56] We also have

$$\alpha_k \zeta_k = \alpha_\ell \zeta_\ell,$$

where ζ_k , ζ_ℓ are the nominal age fields for survey lines k and ℓ (distinct from the data points $\zeta_{ijk\ell m}$). This implies that for every point we can write

$$\alpha_k \zeta_{ijk\ell 1} = \alpha_\ell \zeta_{ijk\ell 2}, \quad (\text{B1})$$

where we have assumed a linear scaling between the nominal ages for each survey line, and the α_i are the scaling parameters. This can be generalized to polynomial relationships between the nominal ages as

$$\sum_\mu \alpha_{k\mu} \zeta_k^\mu = \sum_\mu \alpha_{\ell\mu} \zeta_\ell^\mu,$$

and the equivalent

$$\sum_\mu \alpha_{k\mu} \zeta_{ijk\ell 1}^\mu = \sum_\mu \alpha_{\ell\mu} \zeta_{ijk\ell 2}^\mu.$$

[57] The linear scaling (B1) can be written as the matrix equation

$$(\mathbf{J} - \mathbf{A}(\mathbf{Z})) \mathbf{Z} = 0,$$

where

$$\mathbf{J} = [\mathbf{I}^{N,N}, 0^{N,N}] \in \mathbf{R}^{N,2N}$$

$$\mathbf{A} = [0^{N,N}, \text{diag}(\alpha)] \in \mathbf{R}^{N,2N},$$

where \mathbf{I} and $\mathbf{0}$ represent the identity matrix and zero matrix, respectively, the superscript indicates the dimensions of the

matrix, and $\text{diag}(\alpha)$ represents the diagonal matrix formed from the vector α . Finally, we define a collapse matrix \mathbf{K} with

$$K_{j,(p+1):(p+g_j)} = \mathbf{I}^{1-g_j}$$

$$p = \sum_{k=1}^{j-1} g_k,$$

and with all other entries zero, where we have used ‘‘colon notation’’ [Golub and van Loan, 1989] to indicate the ranges of a series of ordinal numbers. We then define

$$\mathbf{X} = [\mathbf{K}\text{diag}(\mathbf{Z}_2)] \in \mathbf{R}^{M,N}$$

$$\mathbf{L} = [\mathbf{0}^{N,N}, \mathbf{K}\text{diag}(\lambda)] \in \mathbf{R}^{N,2N}.$$

[58] Then, differentiating with respect to the subscript on J

$$J_Z = \mathbf{C}_{Z^*Z^*}^{-1} (\mathbf{Z} - \mathbf{Z}^*) + (\mathbf{J} - \mathbf{A})^T \lambda,$$

$$J_\lambda = (\mathbf{J} - \mathbf{A}) \mathbf{Z},$$

$$J_\alpha = -\mathbf{X},$$

to get the matrix equation for

$$\begin{bmatrix} \mathbf{C}_{Z^*Z^*}^{-1} & (\mathbf{J} - \mathbf{A})^T & \mathbf{0} \\ (\mathbf{J} - \mathbf{A}) & \mathbf{0} & \mathbf{0} \\ \mathbf{0} & -\mathbf{X} & \mathbf{0} \end{bmatrix} \begin{bmatrix} \mathbf{Z} \\ \lambda \\ \alpha \end{bmatrix} = \begin{bmatrix} \mathbf{C}_{Z^*Z^*}^{-1} \mathbf{Z}^* \\ \mathbf{0} \\ \mathbf{0} \end{bmatrix}. \quad (\text{B2})$$

This is a nonlinear equation, owing to the dependence of \mathbf{A} on α and of \mathbf{X} on \mathbf{Z}_2 . The Hessian, which also serves as the Jacobian in the Newton-Raphson iteration of (B2), is given by

$$\begin{bmatrix} \mathbf{C}_{Z^*Z^*}^{-1} & (\mathbf{J} - \mathbf{A})^T & -\mathbf{L}^T \\ (\mathbf{J} - \mathbf{A}) & \mathbf{0} & -\mathbf{X}^T \\ -\mathbf{L} & -\mathbf{X} & \mathbf{0} \end{bmatrix}^q \begin{bmatrix} \delta \mathbf{Z} \\ \delta \lambda \\ \delta \alpha \end{bmatrix}^q = \begin{bmatrix} \rho_Z \\ \rho_\lambda \\ \rho_\alpha \end{bmatrix}^q$$

with the residual at the q th iteration ρ^q given by

$$\begin{bmatrix} \rho_Z \\ \rho_\lambda \\ \rho_\alpha \end{bmatrix}^q = \begin{bmatrix} \mathbf{C}_{Z^*Z^*}^{-1} \\ \mathbf{0} \\ \mathbf{0} \end{bmatrix} - \begin{bmatrix} \mathbf{C}_{Z^*Z^*}^{-1} & (\mathbf{J} - \mathbf{A})^T & \mathbf{0} \\ (\mathbf{J} - \mathbf{A}) & \mathbf{0} & \mathbf{0} \\ \mathbf{0} & -\mathbf{X} & \mathbf{0} \end{bmatrix}^q \begin{bmatrix} \mathbf{Z} \\ \lambda \\ \alpha \end{bmatrix}^q,$$

where the subscripts on ρ now indicate a subvector corresponding to the equations in Z , λ , α . The correction step is

$$\begin{bmatrix} \mathbf{Z} \\ \lambda \\ \alpha \end{bmatrix}^{q+1} = \begin{bmatrix} \mathbf{Z} \\ \lambda \\ \alpha \end{bmatrix}^q + \begin{bmatrix} \delta \mathbf{Z} \\ \delta \lambda \\ \delta \alpha \end{bmatrix}^q,$$

where q refers to the iteration number. The first iteration is performed by taking $\alpha = \mathbf{I}$ and solving (B2) for \mathbf{Z} and λ only.

The solution is the optimal scaling between the nominal ages of individual survey lines that minimizes the errors at crossovers.

[59] Three-dimensional nominal age fields are created by radial basis function interpolation of the nominal age along surfaces of constant *normalized* height using the optimal nominal age defined at regular points along the survey lines.

Appendix C: Optimal Shape-Function Fitting From Arch Size Distribution

[60] We show here how to compute the shape function (vertical velocity distribution) at the divide, given the shape function in a flank area unaffected by horizontal advection. In effect, this means that flanking synclines should not be used [Parrenin and Hindmarsh, 2007]. This method is a subset of a more general method for tracing shape function variations proposed by Rousset *et al.* [2009]. Notation in this appendix is independent of that in the other appendices.

[61] Consider ice with thickness H being recharged by snow accumulation at a rate a . Let the vertical velocity at a divide be given by a shape function $\omega_d(\zeta)$ such that

$$w(\zeta) = -\frac{a}{H} \omega_d(\zeta),$$

and let ω_f denote the corresponding shape function for the flank; subscripts d and f refer to divide and flank in all quantities in this appendix. Then, the one-dimensional equation for the steady age X is

$$-\frac{a\omega_d(\zeta)}{H} \frac{\partial X}{\partial \zeta} = 1,$$

and using the property that X increases monotonically

$$\frac{\partial \hat{\zeta}_d(X)}{\partial X} = -\frac{H\hat{\omega}_d(X)}{a}, \quad (\text{C1})$$

$$\frac{\partial \hat{\zeta}_f(X)}{\partial X} = -\frac{H\hat{\omega}_f(X)}{a}, \quad (\text{C2})$$

where variables with carats indicate that they are functions of X . The rate of change of arch height $\hat{\beta} = \hat{\zeta}_d - \hat{\zeta}_f$ with X (note $\hat{\beta}$ and its cognate β are measured in normalized height) is thus given by

$$\frac{\partial \hat{\beta}(X)}{\partial X} = -\frac{H}{a} (\hat{\omega}_d(X) - \hat{\omega}_f(X)),$$

which can be written

$$\left. \frac{\partial \beta(\zeta)}{\partial \zeta} \right|_{\zeta=\zeta_f} = -\frac{H}{a} (\hat{\omega}_d(X) - \hat{\omega}_f(X)),$$

through use of the chain rule, or, using (C2)

$$\omega_d(\zeta + \beta(\zeta)) = \left(\frac{\partial \beta(\zeta)}{\partial \zeta} + 1 \right) \omega_f(\zeta). \quad (\text{C3})$$

Using the shallow ice approximation to make an assumption about $\omega_f(\zeta)$ and performing say a polynomial fit of β to the data subject to the constraints

$$\begin{aligned}\beta(1) &= 0, \\ \beta(0) &= 0, \\ \left. \frac{\partial\beta(\zeta)}{\partial\zeta} \right|_{\zeta=1} &= 0.\end{aligned}$$

we may compute $\omega_d(\zeta + \beta)$ from (C3). The differential constraint can be seen to arise from (C3) since $\beta(1) = 0$ and by construction the shape functions are unity at the surface.

[62] **Acknowledgments.** Our thanks to Terry O'Donovan for field assistance at Fletcher and, in particular, the technical assistance he gave at Berkner in the field season 2005–2006; to Peter FitzGerald for writing the radar acquisition software; to Oliver Marsh and Hilary Woodard for picking the radargrams; and to Olaf Eisen for a very thorough review and reading. This work was supported by NERC grant NE/F00446X/1 “Measuring and modeling the Raymond Effect for to infer low strain rate ice rheology”.

References

- Bamber, J. L., J. L. Gomez-Dans, and J. A. Griggs, (2009), A New 1 km digital elevation model of the Antarctic derived from combined satellite radar and laser data—Part I: Data and methods, *Cryosphere*, 3, 101–111.
- Bentley, M. J., C. J. Fogwill, A. M. Le Brocq, A. L. Hubbard, D. E. Sugden, T. Dunai, and S. P. H. T. Freeman (2010), Deglacial history of the West Antarctic Ice Sheet in the Weddell Sea embayment: Constraints on past ice volume change, *Geology*, 38, 411–414.
- Bingham, R. G., and M. J. Siegert (2007), Radio-echo sounding over polar ice masses, *J. Environ. Eng. Geophys.*, 12(1), 47–62.
- Buhmann, M. D. (2003), *Radial Basis Functions: Theory and Implementations*, Cambridge Monogr. Appl. Comput. Math., vol. 12, Cambridge Univ. Press, New York.
- Conway, H., and L. A. Rasmussen (2009), Recent thinning and migration of the Western Divide, central West Antarctica, *Geophys. Res. Lett.*, 36, L12502, doi:10.1029/2009GL038072.
- Conway, H., B. Hall, G. Denton, A. Gades, and E. Waddington (1999), Past and future grounding-line retreat of the West Antarctic ice sheet, *Science*, 286, 280–283.
- Gerland, S., H. Oerter, J. Kipfstuhl, F. Wilhelms, H. Miller, and W. D. Miners (1999), Density log of a 181 m long ice core from Berkner Island, Antarctica. *Ann. Glaciol.*, 29, 215–219.
- Golub, G. H., and C. F. van Loan (1989), *Matrix Computations*, 2nd ed., Johns Hopkins Univ. Press, Baltimore, Md.
- Gillet-Chaulet, F., and R. C. A. Hindmarsh (2011), Flow at ice-divide triple junctions: 1. Three-dimensional full-Stokes modeling, *J. Geophys. Res.*, doi:10.1029/2009JF001611, in press.
- Hempel, L., F. Thyssen, N. Gundestrup, H. B. Clausen, and H. Miller (2000), A comparison of radio-echo sounding data and electrical conductivity of the GRIP ice core, *J. Glaciol.*, 46(154), 369–374.
- Jacobel, R. W., and S. J. Hodge (1995), Radar internal layers from the Greenland Summit, *Geophys. Res. Lett.*, 22, 587–590.
- Jacobel, R. W., B. C. Welch, E. J. Steig, and D. P. Schneider (2005), Glaciological and climatic significance of Hercules Dome, Antarctica: An optimal site for deep ice core drilling, *J. Geophys. Res.*, 110, F01015, doi:10.1029/2004JF000188.
- Kaspari, S., P. A. Mayewski, D. A. Dixon, V. B. Spikes, S. B. Sneed, M. J. Handley, and G. S. Hamilton (2004), Climate variability in West Antarctica derived from annual accumulation-rate records from ITASE firn/ice cores, *Ann. Glaciol.*, 39, 585–594.
- Lowitzsch, S. (2005), Error estimates for matrix-valued radial basis function interpolation, *J. Approx. Theory*, 137, 238–249, doi:10.1016/j.jat.2005.09.008.
- Lythe, M. B., D. G. Vaughan, and the BEDMAP Consortium (2001), BEDMAP: A new ice thickness and subglacial topographic model of Antarctica, *J. Geophys. Res.*, 106, 11,335–11,351, doi:10.1029/2000JB900449.
- Martin, C., R. C. A. Hindmarsh, and F. J. Navarro (2006), Dating ice flow change near the flow divide at Roosevelt Island, Antarctica, by using a thermomechanical model to predict radar stratigraphy, *J. Geophys. Res.*, 111, F01011, doi:10.1029/2005JF000326.
- Martin, C., G. H. Gudmundsson, H. D. Pritchard, and O. Gagliardini (2009a), On the effects of anisotropic rheology on ice flow, internal structure, and the age-depth relationship at ice divides, *J. Geophys. Res.*, 114, F04001, doi:10.1029/2008JF001204.
- Martin, C., R. C. A. Hindmarsh, and F. J. Navarro (2009b), On the effects of divide migration, along-ridge flow, and basal sliding on isochrones near an ice divide, *J. Geophys. Res.*, 114, F02006, doi:10.1029/2008JF001025.
- Mulvaney, R., H. Oerter, D. A. Peel, W. Graf, C. Arrowsmith, E. C. Pasteur, B. Knight, G. C. Littot, and W. D. Miners (2002), 1000 year ice-core records from Berkner Island, Antarctica, *Ann. Glaciol.*, 35, 45–51.
- Mulvaney, R., C. Arrowsmith, J. M. Barnola, J. Chappellaz, and R. Hindmarsh (2010), Timing of the late glacial retreat of the Antarctic Weddell Sea ice sheet, *Geophys. Res. Abstr.*, 12, EGU2010-11424.
- Morse, D., E. Waddington, and E. Steig (1998), Ice age storm trajectories inferred from radar stratigraphy at Taylor Dome, Antarctica, *Geophys. Res. Lett.*, 25(17), 3383–3386.
- Nereson, N. A., and E. D. Waddington (2002), Isochrones and isotherms beneath migrating ice divides, *J. Glaciol.*, 48(160), 95–108.
- Nereson, N. A., C. F. Raymond, E. D. Waddington, and R. W. Jacobel (1998), Migration of the Siple Dome ice divide, West Antarctica, *J. Glaciol.*, 44, 643–652.
- Nereson, N. A., C. F. Raymond, R. W. Jacobel, and E. D. Waddington (2000), The accumulation pattern across Siple Dome, West Antarctica, inferred from radar-detected internal layers, *J. Glaciol.*, 46, 75–87.
- Parrenin, F., and R. C. A. Hindmarsh (2007), Influence of a non-uniform velocity field on isochrone geometry along a steady flowline of an ice sheet, *J. Glaciol.*, 53, 612–622.
- Parrenin, F., R. C. A. Hindmarsh, and F. Rémy (2006), Analytical solutions for the effect of topography, accumulation rate variations and flow divergence on isochrone layer geometry, *J. Glaciol.*, 52(177), 191–202.
- Pettit, E. C., and E. D. Waddington (2003), Ice flow at low deviatoric stress, *J. Glaciol.*, 49, 359–369.
- Pettit, E. C., T. Thorsteinsson, H. P. Jacobson, and E. D. Waddington (2007), The role of crystal fabric in flow near an ice divide, *J. Glaciol.*, 53, 277–288.
- Raymond, C. F. (1983), Deformation in the vicinity of ice divides, *J. Glaciol.*, 29, 357–373.
- Raymond, C., B. Weertman, L. Thompson, E. Mosley-Thompson, D. Peel, and R. Mulvaney (1996), Geometry, motion and mass balance of Dyer Plateau, Antarctica, *J. Glaciol.*, 42(142), 510–518.
- Rousselot, M., F. Parrenin, and O. Gagliardini (2009), Reconstruction of 2D and steady-state velocity field of polar ice sheet by inverse modeling of isochrones, *Geophys. Res. Abstr.*, 11, EGU2009-7655-1.
- Steinhage, D., and N. Blindow (1996), First results of short pulse radio echo sounding on the top of Berkner Island, in *10th International FRISP Workshop held at Institut für Angewandte Geodäsie (IfAG), Leipzig, Germany, 11–14 June 1995, FRISP Rep. 9*, pp. 123–126, Filchner-Ronne Ice Shelf Programme, Alfred-Wegener Inst. for Polar and Mar. Res., Bremerhaven, Germany.
- Steinhage, D., O. Eisen, and F. B. Clausen (2005), Regional and temporal variation of accumulation around NorthGRIP derived from ground-penetrating radar, *Ann. Glaciol.*, 42, 326–330.
- Vaughan, D. G., H. F. J. Corr, C. S. M. Doake, and E. D. Waddington (1999), Distortion of isochronous layers in ice revealed by ground-penetrating radar, *Nature*, 398, 323–326.
- Waddington, E. D., H. Conway, E. J. Steig, R. Alley, E. Brook, K. Taylor, and J. White (2005), Decoding the dipstick: Thickness of Siple Dome, West Antarctica, at the last glacial maximum, *Geology*, 33(4), 281–284.
- Wilchinsky, A. V., and V. A. Chugunov (1997), Modelling ice-divide dynamics by perturbation methods, *J. Glaciol.*, 43, 352–358.
- Woodward, J., and E. C. King (2009), Radar surveys of the Rutford Ice Stream onset zone, West Antarctica: indications of flow (in)stability?, *Ann. Glaciol.*, 50(51), 57–62.
- H. F. J. Corr, F. Gillet-Chaulet, G. Hiess, R. C. A. Hindmarsh, E. C. King, and R. Mulvaney, Physical Sciences Division, British Antarctic Survey, Natural Environment Research Council, High Cross, Madingley Road, Cambridge CB3 0ET, UK. (hfjc@bas.ac.uk; fall@bas.ac.uk; gisess@bas.ac.uk; rcach@bas.ac.uk; ecki@bas.ac.uk; rmu@bas.ac.uk)